Journal of Materials Chemistry A

Accepted Manuscript

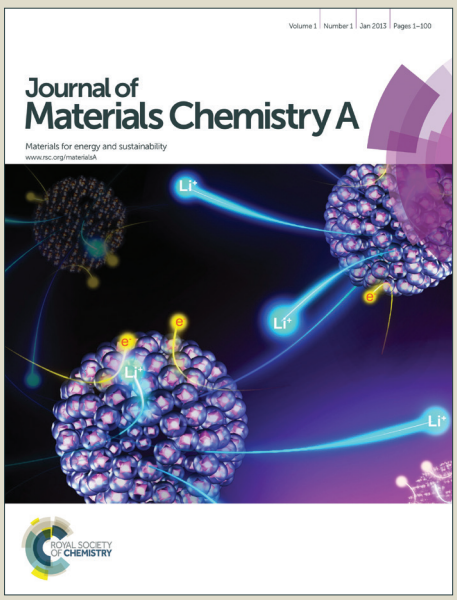

ROYAL SOCIETY OF CHEMISTRY

www.rsc.org/materialsA

Journal Name

RSCPublishing

ARTICLE

Highly Reversible Switching from P- to N-type NO_2 Sensing in Monolayer Fe_2O_3 Inverse Opal and Associated P-N Transition Phase Diagram

Cite this: DOI: 10.1039/x0xx00000x

Received 00th xxxxx, 2014,
Accepted 00th xxxxx, 2014,

DOI: 10.1039/x0xx00000x

www.rsc.org/

Zhengfei Dai,[a] Chul-Soon Lee,[a] Yahui Tian,[a] Il-Doo Kim,[b] and Jong-Heun Lee [a,*]

The detection of nitrogen dioxide, NO_2, is currently the subject of extensive scientific and technological research, motivated by its deleterious impact on the environment and on human health and safety. However, detecting trace levels of NO_2 gas in a timely, sensitive, and selective manner remains challenging, while the mechanisms governing selective NO_2 sensing are still unclear. In this work, a monolayer α-Fe_2O_3 inverse opal (IO) with single-crystalline 3-fold rotocenters is firstly synthesized *in situ* on substrate using a sacrificial template and evaluated as a sensitive NO_2 chemiresistor. Interestingly, the Fe_2O_3 macroporous film manifests abnormal sensing behavior with reversible transitions from p- to n-type sensing as a function of the NO_2 concentration (*C*) and working temperature (*T*). Based on more familiar phase diagrams, a binary (*T*-*C*) transition diagram has been created in terms of the gas sensing response, which can be directly used to design and control the p-n transitions. Further investigations also show that such abnormal p-n transitions do not occur if a different sensing material (*e.g.* SnO_2 IO) is used, or on exposure to gases other than NO_2. The porous Fe_2O_3 sensor is capable of detecting trace levels of NO_2, as low as 10 ppb, and shows good stability. Finally, the mechanisms underlying the unusual NO_2 sensing transitions are described based on the nature of the materials and the well-known Lennard-Jones model. Reversible switching from p- to n-type sensing and the associated transition diagram carry great potential for the recognition and sensitive detection of trace levels of NO_2.

Introduction

The development of industry and automobiles in the past decades has induced the emission of large volumes of soot and toxic gases into the atmosphere, affecting both human health and the environment, and making air pollution a global issue.[1, 2] Nitrogen dioxide (NO_2), one of the most dangerous air pollutants,[3, 4] is mostly released during the combustion of fossil fuels and triggers the formation of ozone, photochemical smog, and acid rain.[5, 6] Trace levels of NO_2 are sufficient to damage the human respiratory system and lung tissues.[7] Ambient air quality standards for NO_2 have been set to 53 ppb (for the annual average) and 100 ppb (for the single-hour average) by the U.S. Environmental Protection Agency (EPA).[8, 9] In this regard, ppb-level NO_2 detection and air quality monitoring are of great significance to public health and the environment.[10, 11] So far, a series of techniques have been developed to detect trace levels of NO_2, including electrochemical, optical, and chemiresistive sensors.[12, 13] Among these, chemiresistors based on semiconducting metal oxides (SMOs) are the most promising due to their irreplaceable merits of low cost, simple fabrication, and good integrated circuit compatibility.[14-16]

In recent years, nanostructured metal oxides have proved to be of great value in gas sensing applications.[17, 18] Downscaling leads to increased surface-to-volume ratios, a larger proportion of near-surface regions with high chemiresistive variation, richer surface active sites, strong adsorption of the target gas molecules, and thereby to enhanced sensing performance.[4, 19, 20] Recently, the detection of trace levels of NO_2 has been reported using SMO sensors based on a rich variety of nanostructures,[21, 22] such as 0-D (zero-dimensional) nanoparticles,[23] 1-D nanowires, and 2-D nanosheets.[24-26] In our previous works, we have shown furthermore that SMO micro/nanopores arrays fabricated by *in situ* templating can serve as ideal sensing films due to their uniform thickness, tunable microstructure, reproducible fabrication, and superior sensitivity to broad range of gases.[27-29] Nevertheless, the wide reactivity of SMO sensors to different gases is often associated with a low selectivity to specific gases, which hampers the practical implementation of chemiresistive sensors.[30] Moreover, detecting trace levels of NO_2 gas in a timely, sensitive, and selective manner remains challenging.

In this context, considerable efforts have been devoted to improve the discrimination ability of SMO sensors, usually by doping [31-33] or surface modification.[34-37] Recently, the discovery of transitions from

p- to n-type gas sensing suggests a new and promising avenue for gas recognition.[38, 39] The n- or p-type gas sensing refers the decrease or increase of sensor resistance upon exposure to reducing gas.[40] To date, the abnormal p–n switching behaviors of metal oxide semiconductors were induced by treatment in a reducing atmosphere[38] or by changes in gas concentration[39] and sample temperature.[41, 42] For instance, Huang *et al.* [39] reported a ZnO-modified SnO_2 nanorod sensor exhibiting concentration-dependent n–p–n transitions in its sensing response to H_2 gas; Wang *et al.* [43] demonstrated abnormal temperature-dependent and concentration-dependent n–p transition behavior in hydrothermally synthesized ZnO nanotube arrays. However, the mechanism and on-demand controllability of such p-n transitions are rarely investigated and remain challenging to understand.

In this work, an n-type monolayer of α-Fe_2O_3 inverse opal (IO) macroporous film is synthesized *in situ* on a sensing substrate using a sacrificial template and is evaluated as a chemiresistive NO_2 gas sensor. This polycrystalline Fe_2O_3 porous thin film has a honeycomb-like morphology, a highly homogenous layout, and single-crystalline 3-fold rotocenter skeletons. Interestingly, the Fe_2O_3 porous film, an n-type material, demonstrates abnormal sensing behavior with reversible switching from p- to n-type NO_2 sensing tuned by the NO_2 concentration (*C*) and working temperature (*T*). Further, a binary (*T*-*C*) transition diagram has been created for the first time on the basis of the NO_2 sensing response, which can be directly used to design and tailor the p-n transitions. In comparison with similar SnO_2 structures and to the sensing of other gases, this study suggests that these p-n transition characteristics are unique to NO_2 sensing with this porous Fe_2O_3 film. The device developed here is able to detect NO_2 at levels as low as 10 ppb. This discovery of highly reversible p-n sensing and the description of the associated transition diagram may open up interesting possibilities in the selective detection of trace levels of NO_2.

Experimental section

Preparation of Monolayer Porous Films

Glass slides, 7.5×2.5 cm^2 and 2 mm thick, were cleaned as reported previously.[14a] A suspension of monodispersed polystyrene spheres (PS) 500 nm in diameter (2.5 wt% in water) was purchased from Alfa Aesar. The PS suspension was diluted in the same volume ethanol and ultrasonicated for absolute uniformity. A PS colloidal monolayer template was prepared on the well-cleaned glass slide by air/water interfacial assembly. [27] In brief, a cleaned glass slide was first placed on a flat table and subsequently covered with deionized water on the surface of the slide (about 2 mm in thickness); second, the ethanol-diluted PS suspension (ca. 50 μL in volume) was slowly injected into the water at the edge of the pre-formed water-film for about 5 min; after injection, we kept it for 5 min for PS spheres' self-assembly at the air/water interface; finally, the large-area monolayer was formed on the slide after liquid evaporation. The precursor solution was 0.1 M aqueous $Fe(NO_3)_3$. As depicted in Figure S1**,** the slide is slowly dipped into the aqueous $Fe(NO_3)_3$ solution (Figure S1a). Integral monolayers then detach from the glass substrate and float on the surface of the solution (Figure S1b), ready to be attached to the desired substrate (Figure S1c).[28] Here alumina sensor substrates were used with two Au electrodes (widths: 0.25 mm, separation: 0.15 mm) and a microheater on the underside. These were flat-placed for 10 min then dried at 110 °C for 0.5 h in an oven (Figure S1d). This PS bead coating process is robust and can therefore be accomplished successfully regardless of the type of substrate.[27-29] Finally, the dried substrate covered with the PS monolayer was transferred into a furnace and kept at 600 °C for 3 h to burn the PS spheres away and form porous honeycomb-like Fe_2O_3 thin films (Figure S1e–f).

Characterization

The morphology and microstructure of the samples were examined using field emission scanning electron microscopy (SEM, S-4700, Hitachi Co. Ltd, Japan) and transmission electron microscopy (TEM, JEM-ARM-200F, JEOL, USA). An analysis of the phases present in the films was carried out using grazing incidence X-ray diffraction (XRD, D/MAX-2500V/PC, Rigaku, Japan) using Cu Kα (0.15419 nm) radiation with an incidence angle of 0.3°. X-ray photoelectron spectroscopy (XPS) was conducted using an Al Kα X-ray source in a Thermo-VG MULTILAB 2000 spectrometer.

Gas-Sensing Measurements

Sensor devices were built by in-situ fabrication of ordered porous thin films on the above-mentioned alumina substrates. Gas sensing experiments were carried out in a dynamical gas sensing system. The sensor temperatures were controlled using the micro-heater attached to the underside of the substrate and measured using an IR temperature sensor (Metis MP25, Sensortherm GmBH, Germany). The gas concentrations were controlled independently by mixing gases and dry air, and a constant flow rate of 500 sccm was employed. Throughout the entire experiment to measure the gas response, the O_2/N_2 ratio (21:79) was kept constant to avoid the chemiresistive variation due to the change of oxygen concentration. The sensing response was obtained by measuring variations of electrical current in the sensing devices using a Keithley 6487 picoammeter.

Results and Discussion

Monolayered Fe_2O_3 inverse opal (IO)

A sacrificial monolayer template was employed to synthesize Fe_2O_3 IO porous thin films *in situ*, as illustrated in Figure S1. In brief, a glass slide is first covered with a polystyrene (PS) colloidal monolayer by air/water interfacial self-assembly (Figure S2).[27] A $Fe(NO_3)_3$ aqueous solution is used as the precursor solution. Based on the solution-dipping route shown in Figure S1, the PS monolayer floating on the solution surface is attached to the desired substrate,[28] such as a silicon wafer, glass, metal grid, or alumina sensor. During the subsequent heat treatment, the PS spheres are burned off while honeycomb-like Fe_2O_3 IO porous thin films are directly formed on the substrate.

A typical SEM image of a self-organized PS colloidal sphere monolayer is presented in Figure 1a. The monolayer is composed of PS spheres (500 nm in diameter) in a hexagonal close-packed arrangement. Distinct and uniform hexagonal spots are observed in the two-dimensional (2D) Fourier transform patterns—obtained using a fast Fourier transformation (FFT) filter in the image processing software (inset in Figure 1a)—indicating that the PS monolayer exhibits long-range order in keeping with a hexagonally ordered arrangement. The high-magnification SEM image in Figure 1b further confirms the hexagonal close-packed arrangement and the presence of a monolayer (Figure 1b inset). This high-quality colloidal sphere monolayer should ensure a superior film with good homogeneity. Figure S2b presents a photograph of the as-synthesized Fe_2O_3 IO porous thin film on the Si substrate prepared using the aforementioned *in situ* sacrificial template strategy. The sample is iridescent due to the diffraction effect of the thin film,

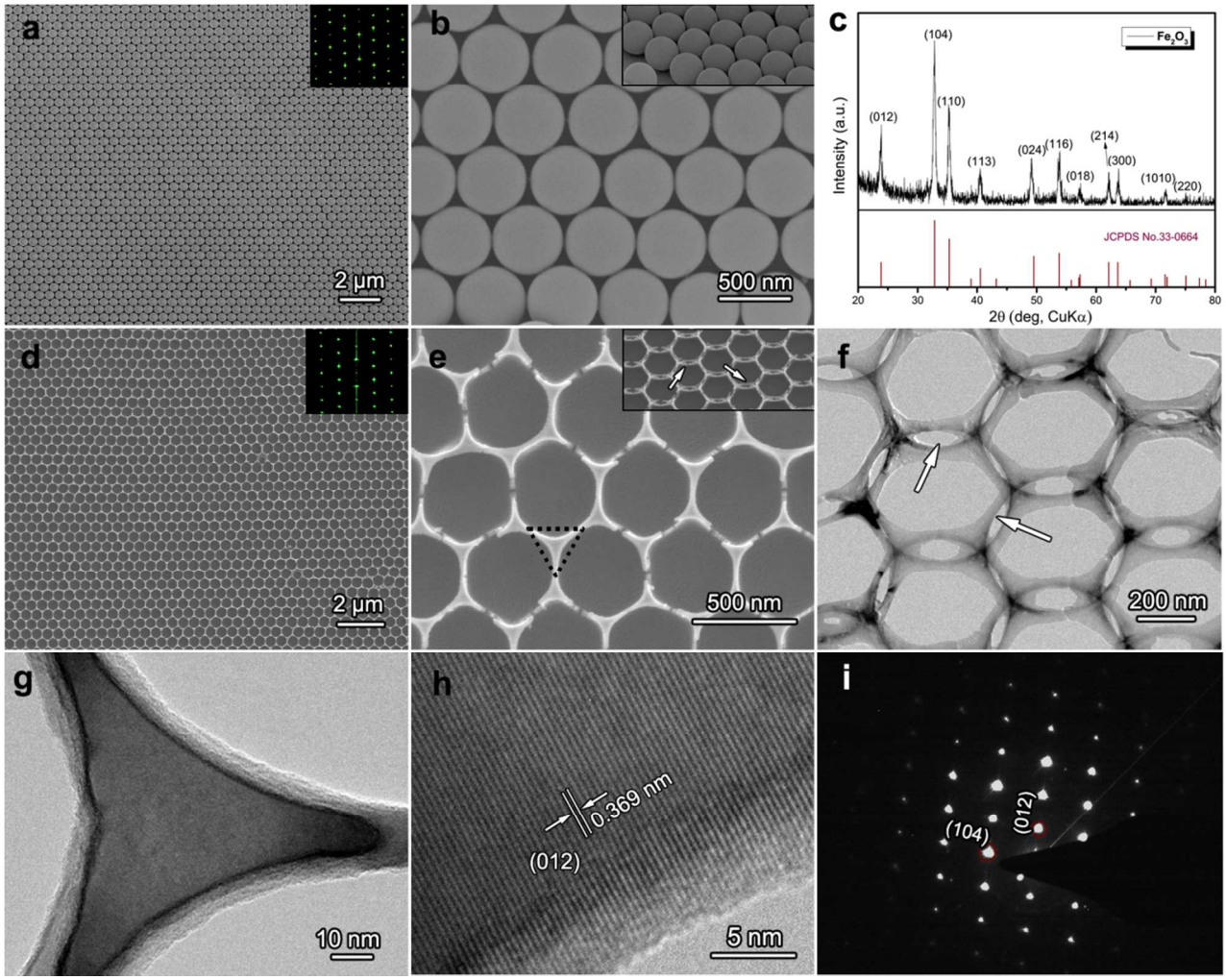

Figure 1. Microstructural characterization of template-directed Fe_2O_3 porous thin films. (a) A typical SEM image of a PS microsphere monolayer on a Si substrate; (b) a high-magnification SEM image of a PS monolayer; (c) XRD pattern obtained from the as-synthesized Fe_2O_3 porous film; (d, e) SEM images of an Fe_2O_3 porous film, in (d) regular and (e) high magnification; (f, g) TEM images of an Fe_2O_3 porous film, with (g) showing the area marked by a dotted triangle in (e); (h) HRTEM image and (i) SAED pattern from an Fe_2O_3 porous film. The insets in (a) and (d) show the corresponding Fourier transform images, while the insets in (b) and (e) show 45°-tilted side views.

highlighting the formation of periodic pore arrays. In the XRD pattern, no preferred orientation was found, and the relative intensities of the peaks are well matched with the standard JCPDS card (No. 33-0664), indicating the as-synthesized Fe_2O_3 porous thin film as polycrystalline α-Fe_2O_3 phase, as shown in Figure 1c.

The morphology and microstructure of the template-directed Fe_2O_3 porous thin films were also investigated (Figure 1d–i). The template-directed Fe_2O_3 porous thin film (Figure 1d) is visually crack-free, and characterized by a homogenous honeycomb-like array. The corresponding 2D FFT (Figure 1d inset) indicates long-range order in the film, consistent with the hexagonally ordered pore arrangement, and emphasizing a perfect template replication process. This is further confirmed by the corresponding high-magnification SEM image (Figure 1e). The cross-sectional image (see Figure S3a) readily shows that the Fe_2O_3 IO monolayer is about 188 nm thick. The corresponding SEM image taken at a tilted angle of 45º also displays a porous array with via holes (marked with arrows in the inset of Figure 1e). This geometrical via-hole structure is further elucidated by the TEM images in Figure 1f. In accordance with the SEM features, hexagonally ordered pores are apparent; meanwhile, *via*-holes are observed between each adjoining set of pores (marked with arrows in Figure 1f). These *via*-holes are caused by the increase in contact area between two adjacent PS spheres (from point contact to area contact), upon drying the samples at 110 °C, near the glass-transition temperature of the PS spheres.[44, 45] In addition, the energy-dispersive X-ray (EDX) spectrum indicates that the porous thin films consist of Fe and O with an atomic ratio of 1:1.55 (see Figure S3b). Note that the Au peaks are from the Au TEM grid.

Figure 1g shows the microstructure of the pore skeleton in the 3-fold rotocenter marked with a dotted black triangle in Figure 1e. The high-resolution TEM (HRTEM) image in Figure 1h clearly shows the Fe_2O_3 grains with a fringe spacing of 0.369 nm corresponding to the (012) plane. Interestingly, the corresponding selected-area electron diffraction (SAED) pattern confirms the single-crystalline structure of the skeleton surrounding the Fe_2O_3 pores suggested in Figure 1i. The single-crystal lattice may arise from the intrinsic characteristics of the colloidal sphere template method by which the skeleton or wall of the honeycomb-like pore is confined to the interstices between the close-packed PS spheres. However, this result is seemingly in disagreement with the XRD pattern, which

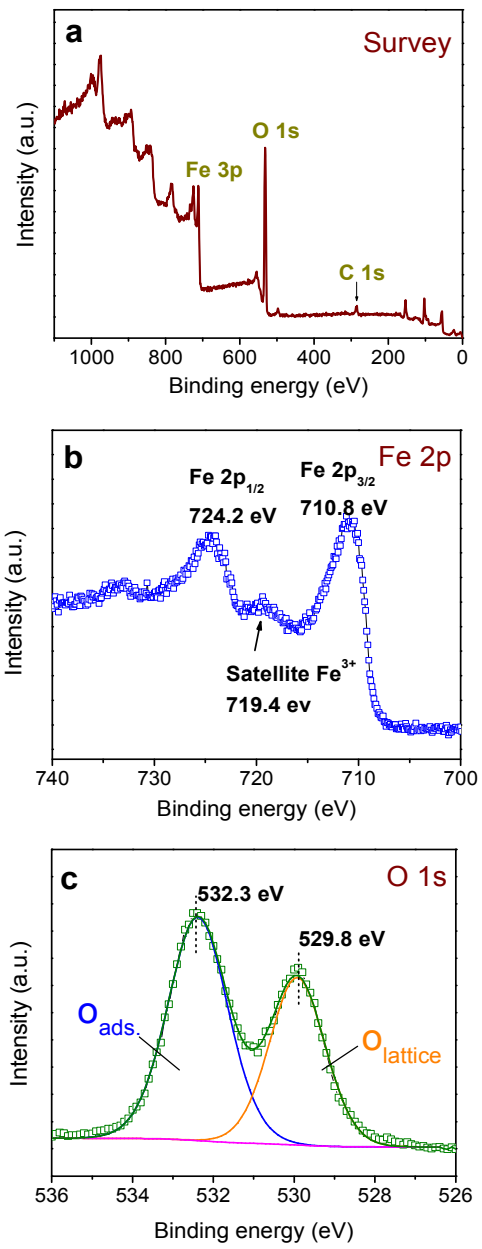

Figure 2. XPS spectra obtained from Fe_2O_3 porous films. (a) A survey spectrum, (b) an Fe 2p binding energy spectrum, and (c) an O 1s core level spectrum.

indicates a polycrystalline film structure. The microstructure was therefore investigated in greater detail using HRTEM, as shown in Figure S4. In the channel between two single-crystalline 3-fold rotocenters, different crystal domains are observed, as marked with yellow arrows in Figure S4c, leading overall to a polycrystalline structure. Thus, the Fe_2O_3 IO monolayer film consists of monolayer building blocks built around multiple single-crystalline 3-fold rotocenters. For metal oxide chemiresistors, high temperatures are usually required to activate the gas sensing reaction. High-temperature measurements always lead to a certain amount of grain growth, which has a negative impact on for the sensing stability of SMO sensors.[8] In this context, the good stability of our uniformly porous structure, associated with the single-crystalline 3-fold rotocenters in the pore skeleton, may afford superior sensing performances.

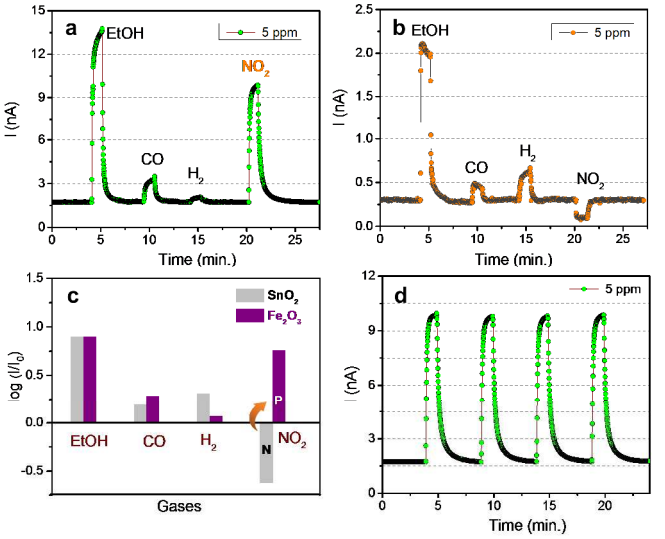

Figure 3. The gas sensing properties of Fe_2O_3 and SnO_2 porous thin films at 450 °C. (a) Dynamic sensing transients measured in (a) an Fe_2O_3 and (b) a SnO_2 porous film exposed to 5 ppm of different gases. (c) A bar graph summarizing the data shown in (a) and (b). (d) The sensing responses of the Fe_2O_3 porous film over 4 cycles of exposure to 5 ppm NO_2.

The chemical composition and the valence state of the elements in the Fe_2O_3 porous thin film were examined by XPS. Figure 2a shows a typical XPS survey spectrum in the Fe 2p, O 1s, and C 1s regions for the Fe_2O_3 film. The binding energies obtained from the XPS analysis were corrected for specimen charging by referencing the C 1s line to 284.5 eV. In the Fe 2p spectrum (Figure 2b), two distinct peaks are observed at binding energies of ~710.8 eV for Fe $2p_{3/2}$ and ~724.2 eV for $Fe2p_{1/2}$ with a shake-up satellite at ~719.4 eV, which are characteristic of Fe^{3+} ions in their oxide form.[46] The valence state of +3 is feasible considering the high –heat treatment temperature (600 ºC, 3h in air). Results from the deconvolution of the O 1s binding energy spectrum suggest two peaks at 529.8 and 532.3 eV (Figure 2c) that are attributed to lattice oxygen $O_{lattice}$ (O^{2-}) and surface adsorbed oxygen O_{ads} (*e.g.* O^-).[47] For comparison furthermore, porous thin films of tin oxide (a typical n-type sensing material) were synthesized using the same template dipping route (see Figure S5). No single-crystalline skeleton is apparent from their characterization. Moreover, the relative intensity of $[O_{ads}]/[O_{lattice}]$ in the SnO_2 films (Figure S5d) is clearly lower than in our Fe_2O_3 sample (Figure 2c), which indicates a larger population of surface oxygen species in the Fe_2O_3 porous film.

P-N sensing transition

Based on the strategy outlined in Figure S1, we deposited the honeycomb-like single-crystalline skeletoned Fe_2O_3 IO porous thin films *in-situ* on alumina substrate with two Au electrodes and a microheater to produce gas sensing devices. The gas sensing experiments were carried out by sequential exposure of the sensors to various gases in a dynamical gas sensing system. The sensing response was obtained by measuring the change of the electrical current (I) of the sensing devices using a picoammeter (Keithley, Model 6487) with an inter-electrode bias voltage of 3 V. The exposure time was 1 min for each gas sensing event. Figure 3a presents the dynamic sensing transients of the porous Fe_2O_3 thin film sensor exposed to 5 ppm of different gases at 450 °C. Increased current or conductance is observed for reducing gases such as EtOH, CO, and H_2, as expected for n-type semiconducting metal oxides.

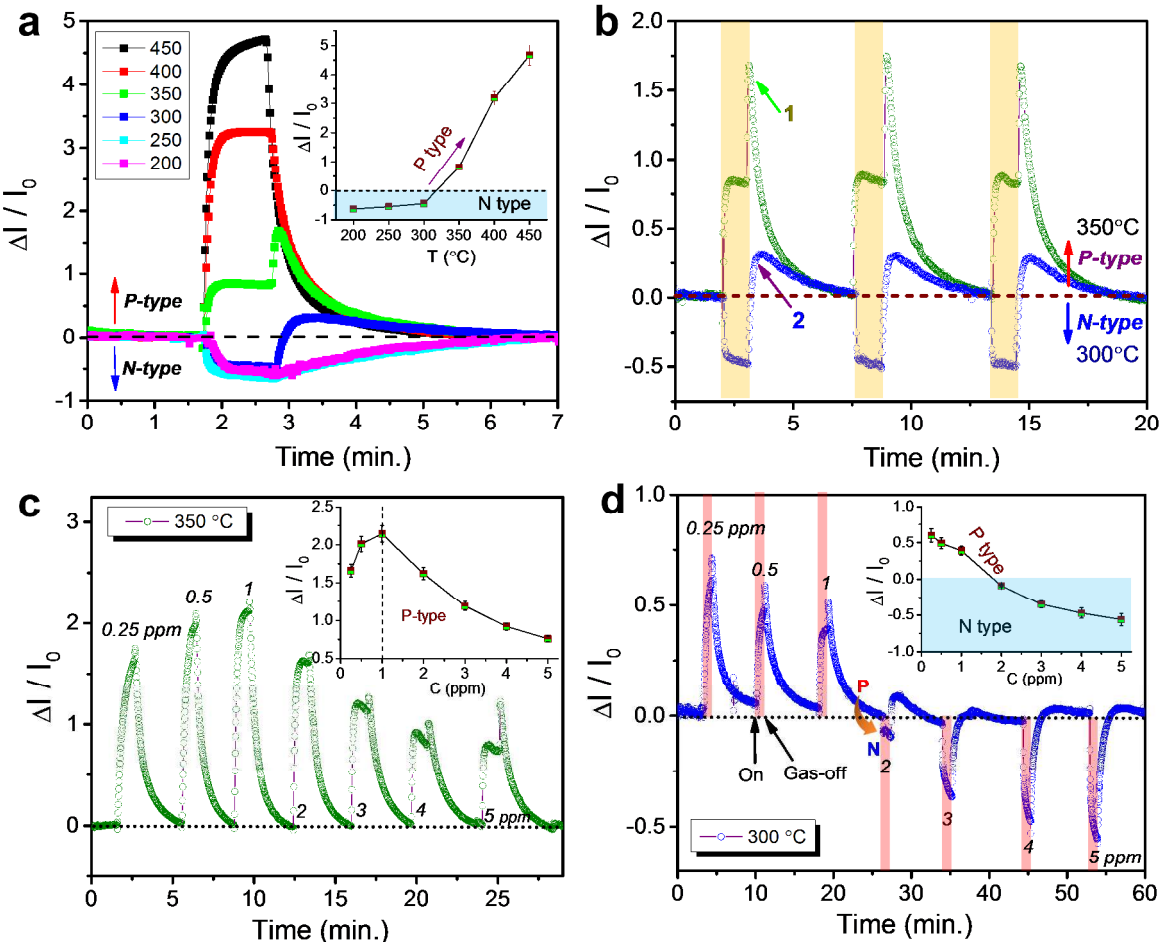

Figure 4. The NO_2 sensing properties of the Fe_2O_3 porous film at different *T* and *C*. (a) The dynamic sensing transients measured on exposure of the film to 5 ppm NO_2 for *T* ranging from 200 to 450 ºC. (b–d) Sensing responses (b) over 3 cycles of exposure to 5 ppm NO_2 at 300 and 350 ºC, (c) to 0.25–5 ppm NO_2 at 350 ºC, and (d) to 0.25–5 ppm NO_2 at 300 ºC. The insets in (a), (c), and (d) show the corresponding *S*-*T*, *S*-*C,* and *S*-*C* dependencies, respectively.

However, an abnormal current increase occurs on exposure to oxidizing NO_2 gas. Chemiresistive sensors are classified as n- or p-type depending on whether their conductance increases or decreases when they are exposed to a reducing gas, and vice versa for oxidizing gases, *i.e.* decreased conductance is expected for n-type sensing.[40] In this context, the porous Fe_2O_3 thin film exhibits an unusual p-type gas sensing response to NO_2, more like that of a p-type metal oxide.

To verify the specificity of the p-n transition in these Fe_2O_3 films, the sensing behavior of the SnO_2 ordered porous thin film, a typical n-type sensing material,[48, 49] was also investigated, as shown in Figure 3b, to see whether p-type NO_2 sensing also occurs. The n-type SnO_2 sensor displays normal n-type sensing responses to all the gases. The bar plot in Figure 3c compares the logarithmic current ratios, I/I_0 (I_0, the current in air), of the two sensors to different gases, highlighting the unique anomalous p-type sensing to NO_2 of the porous Fe_2O_3 thin film sensor, with $\log(I/I_0) > 0$. Figure 3d plots the stable p-type sensing characteristics of this device over 4 cycles of exposure to 5 ppm NO_2 at 450 ºC. Here the response time, defined as the time taken to reach a 90% variation in current upon gas exposure, is as fast as ~12 s. This anomalous p-type sensing behavior may prove extremely useful in chemosensing nanodevices for NO_2 gas recognition.

Influence factors and transition diagram.

While a great deal of attention has been devoted to p-n transition for gas selectivity, few studies have focused on the key parameters governing the transition and how to control it reversibly. Herein, we have investigated the dependence of the p-n transition on the working temperature (*T*) and the NO_2 concentration (*C*). In this study, the sensor signal (*S*) or response is defined as $\Delta I/I_0$, where ΔI stands for the current variation $(I-I_0)$. This parameter is positive (negative) for p-type (n-type) NO_2 sensing. Figure 4a presents the 5 ppm-NO_2 sensing response transients over a range of temperatures from 200–450 °C. The sensing response at 450 °C is higher than at the other working temperatures. Importantly, the Fe_2O_3 sensor undergoes reversible p-n switching as a function of *T*, as shown in Figure 4a. Below 300 °C, the Fe_2O_3 film preserves its intrinsic n-sensing characteristics with $S < 0$, typical of an n-type metal oxide, while anomalous p-sensing behavior is observed with $S > 0$ when $T \geq 350$ °C. The *S vs. T* relationship is illustrated in the inset of Figure 4a, clearly showing the n-p transition that occurs with increasing temperatures. Figure 4b further confirms the switch from p- to n-type behavior close to the transition temperature, with stable p- and n-type sensing over 3 cycles of exposure to 5 ppm NO_2, at 350 ºC and 300 ºC, respectively. In addition, two interesting features are

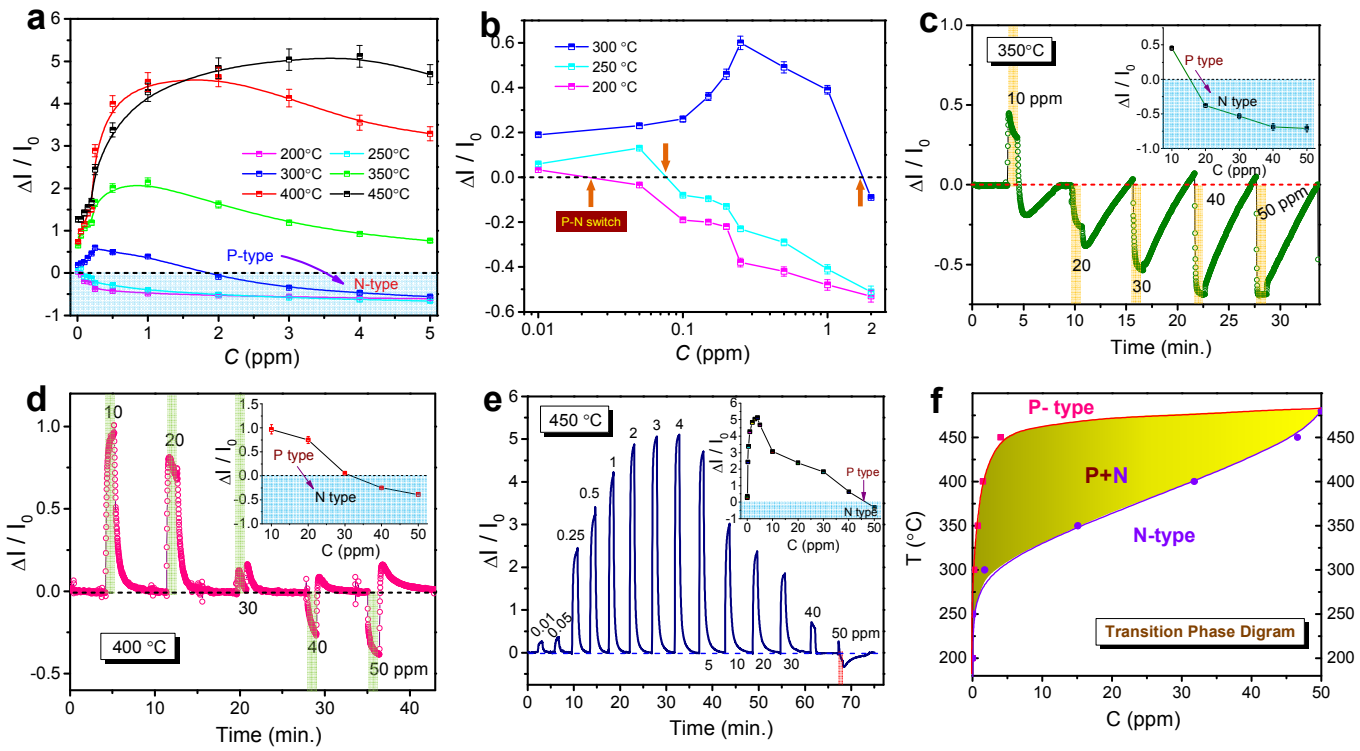

Figure 5. The NO_2 sensing properties of the Fe_2O_3 porous film and its p-n transition diagram. (a, b) Sensing signals on exposure to (a) 0.01–5 ppm NO_2 at 200–450 ºC, and to (b) 0.01–2 ppm NO_2 at 200–300 ºC. Transitions from p- to n-type sensing are indicated by arrows in (b). (c–e) NO_2 sensing responses at 350, 400, and 450 ºC, with the corresponding S-C curves as insets. (f) The T-C transition phase diagram.

observed in Figure 4b, namely an increased $\Delta I/I_0$ ratio (see arrow 1), and an excessive recovery peak (see arrow 2) when the device is refreshed in air. These will be explained in the next section. In summary, these results show that reversible p- to n-type NO_2 sensing transitions can be induced through temperature modulation.

At fixed sensor temperatures, the gas concentration may also influence the sensing response. We measured the NO_2 sensing response in the range of 0.25–5 ppm at different temperatures, as shown in Figure 4c-d and Figure S6. At 350 °C, as the gas concentration is increased, sensing response increases at first but then decreases (Figure 4c), while a normal monotonous increase in $|S|$ is observed with increasing NO_2 concentration at 200 and 250 °C (see Figure S6a-b). The inset of Figure 4c shows the sensing signal (S) as a function of the NO_2 concentration, with the peak p-type sensing response occurring at a concentration of 1 ppm at 350 °C. The behavior is similar at higher T, as shown in Figure S6c-d, where the concentrations giving the maximum NO_2 responses are 2 and 4 ppm at 400 and 450 °C, respectively. In the 0.25–5 ppm range, no p-n transitions occur between 200–250 °C (where n-type sensing is observed) and 350–450 °C (where p-type sensing is observed). However, a clear switch from p- to n-type sensing occurs in the 0.25–5 ppm range at 300 °C, as shown in Figure 4d. For NO_2 concentrations of 0.25–1 ppm, abnormal p-type sensing is observed, whereas the sensor behaves as an n-type sensor in the 2–5 ppm range. The transition from p- to n-type behavior is shown in the Figure 4d inset, with S plotted as a function of C. At lower T (*e.g.* 200 and 250 °C), these transitions can also be observed by varying the concentration (Figure S7).

In Figure 5a, S is plotted at different temperatures for NO_2 concentrations ranging from 0.01–5 ppm. At low T (≤ 300 °C), the sensor undergoes a transition from p- to n-type with increasing NO_2 concentration (C). An expanded view of the 0.01–2 ppm range at low T (≤ 300 °C) is shown in Figure 5b, clearly showing that the concentration at which the transition occurs (indicated with arrows) increases with T. At high T (> 300 °C), the trends in Figure 5a suggest that a transition from p- to n-type sensing behavior occurs at higher NO_2 concentration. Figure 5c-e present the response of the sensor to NO_2 at an increased C of 50 ppm at 350, 400, and 450 °C. The insets show the corresponding S-C relationships, where the transition occur between 10 and 20 ppm at 350 °C, 20 and 30 ppm at 400 °C, and 40 and 50 ppm at 450 °C. At 450 °C, the threshold concentration for detection is as low as 10 ppb (Figure 5e). On the contrary, no p-n transition is observed in Figure S8 for the SnO_2 sensor exposed to 0.05–50 ppm NO_2 at 200–450 °C. The finding of reversible switching from p- to n-type sensing with the variation of T and C can be used as a new strategy for selective NO_2 detection. For instance, the gas response of this sensor could be measured at two different temperatures using pulsed heating with two different heater voltages. The sensor signal ($\Delta I/I_0$) at temperatures ≤ 250 °C and ≥ 350°C would be of opposite sign on exposure to NO_2 but of the same sign for other reducing gases. This provides a novel and simple NO_2 recognition mechanism.

As revealed above, p- or n-type gas sensing can be selected in the porous Fe_2O_3 device by adjusting the operating temperature (T) or the NO_2 gas concentration (C). Taking the sensing behavior as a "phase", a transition phase diagram can be established from the data shown in Figures 4 and 5. According to Gibbs' phase rule, there are two degrees of freedom (f) at constant pressure, T and C. The transition phase diagram is plotted in Figure 5f. For a pure p-type or n-type sensing, the absolute sensor signal ($|\Delta I/I_0|$) should normally increase with the gas concentration. However, with the increasing NO_2 concentration (C), the Fe_2O_3 sensor showed the p- to n- type sensing transition (see the blue curve in Figure 5a), and the process can be successively divided into three stages: (i) $\Delta I/I_0>0$, $\Delta I/I_0$

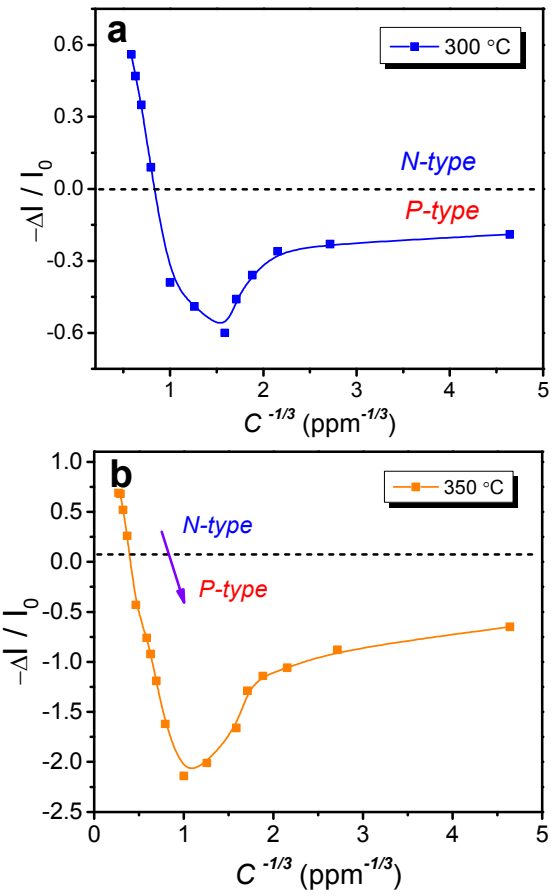

Figure 6. $(-\Delta I/I_0)$ as a function of $C^{-1/3}$ at (a) 300 ºC and (b) 350 ºC for the porous Fe_2O_3 thin film sensor.

increased with C (typical p-type); (ii) $\Delta I/I_0>0$, $\Delta I/I_0$ decreased with C (abnormal type); (iii) $\Delta I/I_0<0$, $|\Delta I/I_0|$ increased with C (typical n-type). Herein, the abnormal (ii) stage is defined as a p+n mixed sensing behavior. The red curve indicates the peak C at different T, above which the sensor behaves as a normal p-type sensor, with S increasing with C. On the other hand, the violet curve delimits the region in which n-type sensing behavior is observed, with the conductance decreasing on exposure to NO_2 (i.e. S decreases with increasing C). The two curves divide the diagram into 3 regions, the p-zone, n- zone, and the p+n mixed phase zone. The transition phase diagram facilitates the identification of the sensing that corresponds to different T and C. Such a T-C transition phase diagram can guide the design of SMO sensors tuned accurately and as desired through an appropriate choice of T and C. In addition, Figure S9 highlights the good sensing stability and the reliability of the single-crystalline skeletoned porous Fe_2O_3 porous thin film over 4 weeks, as required for a commercially viable sensing device.

Transition Mechanism

Although switching from p- to n-type NO_2 sensing has been reported previously for some metal oxides,[43, 50, 51] the mechanism governing the sensing transition has so far not been systematically described. For our Fe_2O_3 sensor, at a given T, the $\Delta I/I_0$ ratio increases at first (and is positive) before gradually decreasing and becoming negative with increasing NO_2 concentrations. This behavior is akin to the classical Lennard-Jones (LJ) potential function that relates the separation (r) of two molecules to their potential energy (E) arising from intermolecular attractive and repulsive forces,[52, 53] as shown in Figure S10. Since r is proportional to $C^{-1/3}$, we have plotted the

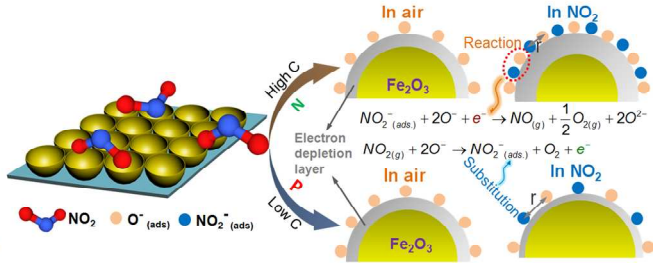

Figure 7. A schematic illustration of the mechanism governing the transitions from p- to n-type NO_2 sensing in the porous Fe_2O_3 thin film.

corresponding $(\Delta I/I_0)$ *vs.* $C^{-1/3}$ curves at typical transition temperatures of 300–350 °C (Figure 6). Interestingly, $(\Delta I/I_0)$ *vs.* $C^{-1/3}$ follows a LJ-type curve, with a characteristic decrease–(negative) trough–increase evolution as a function of C (Figure S10). For NO_2 sensing with SMO chemiresistors, the surface chemisorbed $O^-_{(ads)}$ and $NO_2^-_{(ads)}$, as well as their interactions, have a significant impact on the sensing properties, as illustrated by the following reactions.[54]

$$O_2(g) + 2e^- \rightarrow 2O^-_{(ads.)} \quad (1)$$

$$NO_2(g) + e^- \rightarrow NO_2^-_{(ads.)} \quad (2)$$

Herein, a plausible mechanism is proposed to explain the abnormal p-n transition observed in this device, based on the assumption that the $O^-_{(ads)}$ and $NO_2^-_{(ads)}$ behave like two molecules in a LJ potential, as shown in Figure 7. When the sensor is placed in air, oxygen molecules adsorb on the film surface to form $O^-_{(ads)}$ ions by capturing electrons from the conductance band, leading to the formation of an electron depletion layer and thus to an increase in the resistance of the sensing body (reaction (1)). After exposure to NO_2 gas, this can directly adsorb on the surface leading to reaction (2). For low NO_2 concentrations, the $O^-_{(ads)}$ and $NO_2^-_{(ads)}$ ions are normally too far apart to interact. Because our Fe_2O_3 porous film is superrich in $O^-_{(ads)}$, with $[O_{ads}]/[O_{lattice}] > 1$ (see Figure 2c), this suggests that there are no surface active sites available for NO_2 gas adsorption. In this context, the formation of $NO_2^-_{(ads)}$ mainly occurs by substitution of $O^-_{(ads)}$. Therefore, the balance between reaction (1) to reaction (2) governs the final sensing behavior. The general process is described in the following reaction whereby electrons are simultaneously fed back into the sensing body, leading to increased conductance and thereby to abnormal p-type NO_2 sensing behavior.

$$NO_2(g) + 2O^-_{(ads.)} \rightarrow NO_2^-_{(ads.)} + O_2(g) + e^- \quad (3)$$

Furthermore, the excessive recovery (indicated by arrows in Figure 4b) during the first stage of exposure to air probably arises from each $NO_2^-_{(ads)}$ ion transforming rapidly into NO_2 gas and releasing one electron back into the film. Subsequent decrease of current can be attributed to the occupying of negatively charged surface oxygen ($O^-_{(ads.)}$) instead of previous $NO_2^-_{(ads.)}$. That is, this can be explained by the one-electron response, one-electron initial recovery, and two-electron eventual recovery. When the sensor is exposed to high concentrations of NO_2, the $NO_2^-_{(ads)}$ will not only replace the $O^-_{(ads)}$, but also lead to surface adsorbed active site redistribution. By definition, the distance between the $O^-_{(ads)}$ and $NO_2^-_{(ads)}$ ions is shorter, such that they interact as described in reaction (4).[55] The lower partial pressure of oxygen makes reaction (4) more favorable, whereby electrons are captured from the film, lowering its conductance as in a normal n-type NO_2 sensor.

$$NO_{2\ (ads.)}^{-} + 2O^{-} + e^{-} \rightarrow NO(g) + \frac{1}{2}O_2(g) + 2O^{2-} \quad (4)$$

The competition between reactions (3) and (4) governs the transitions between p- and n-type sensing. At high NO_2 concentrations, reaction (4) dominates so that n-type sensing is observed (see Figure 7).

The reason why this material can also undergo *T*-modulated p-n transitions is addressed in the following. As is well known, the majority charge carriers and the number of surface oxygen anions vary significantly between different oxide semiconductors. Among n-type oxide semiconductors, Iwamoto *et al.* have shown that multivalent transition metal oxides such as Fe_2O_3 adsorb more surface oxygen than other n-type metal oxides (such as SnO_2).[56, 57] The XPS analysis of Fe_2O_3 and SnO_2 (see Figures 2 and S5d) is in good agreement with the above finding. Thus, the p-n transitions associated with reactions (3) and (4) are related to the superrich $O^{-}_{(ads)}$ ions in the porous Fe_2O_3 thin films. At higher *T*, the amount of surface-adsorbed oxygen increases,[56, 57] such that higher $NO_2^{-}{}_{(ads)}$ concentrations are required to match and facilitate reaction (4) and confer normal n-type sensing characteristics. This explains the higher concentrations at which the transition occurs at high temperatures, as highlighted in the transition phase diagram in Figure 5e. This distinctive LJ-like model is a novel way to understand and tune transitions from p- to n-type NO_2 sensing.

Conclusions

To summarize, an n-type α-Fe_2O_3 monolayer inverse opal thin film was synthesized *in situ* on an alumina sensor substrate using a sacrificial monolayer template and evaluated as a chemiresistive NO_2 gas sensor. The polycrystalline Fe_2O_3 porous thin film has a honeycomb-like morphology with a highly uniform layout built around a skeleton of single-crystalline 3-fold rotocenters, affording fast and sensitive gas detection. Interestingly, the Fe_2O_3 porous film, an n-type material, displays abnormal and reversible transitions from p- to n-type NO_2 sensing as a function of the NO_2 concentration (*C*) and the working temperature (*T*). Similar to a phase diagram, a binary (*T*-*C*) transition diagram has been created based on the gas sensing response, which can be directly used to design and control these p-n transitions. It should be emphasized that this behavior is unique to the porous Fe_2O_3 film studied here. Indeed, a similar device based on SnO_2 shows normal n-type sensing characteristics. The porous Fe_2O_3 sensor is capable of detecting NO_2 at concentrations as low as 10 ppb, and shows good stability. Finally, a mechanism is proposed to explain the NO_2 sensing transitions based on the nature of the materials and the well-known Lennard-Jones model. This reversible switching from p- to n-type sensing and the corresponding transition diagram carries great potential for the recognition and sensitive detection of trace levels of NO_2.

Acknowledgements

This work was supported by the National Research Foundation of Korea (NRF) (No. 2013R1A2A1A01006545)

Notes and references

[a] Department of Materials Science and Engineering, Korea University, Seoul 136-713, Republic of Korea;

[b] Department of Materials Science and Engineering, Korea Advanced Institute of Science and Technology, Daejeon, 305-701, Republic of Korea

* Give contact information for the author(s) to whom correspondence should be addressed: jongheun@korea.ac.kr.

Electronic Supplementary Information (ESI) available: Fabrication illustration for Fe_2O_3 IO; photographs of PS templated Fe_2O_3 IO; SEM and TEM image and EDS pattern; characterization of SnO_2 IO; sensing responses to trace NO_2 of Fe_2O_3 IO; NO_2 responses of SnO_2 IO sensor; bar graphs of the sensing signals to NO_2 and CO; sensor stability over 4 week; schematic illustration of the LJ potential.. See DOI: 10.1039/b000000x/

1. M. Ammann, M. Kalberer, D. Jost, L. Tobler, E. Rössler, D. Piguet, H. Gäggeler and U. Baltensperger, *Nature*, 1998, **395**, 157-160.
2. S. H. Lim, L. Feng, J. W. Kemling, C. J. Musto and K. S. Suslick, *Nat. Chem.* 2009, **1**, 562-567.
3. C. Haisch and R. Niessner, *Anal. Chem.* 2012, **84**, 7292-7296.
4. M. C. McAlpine, H. Ahmad, D. Wang and J. R. Heath, *Nat. Mater.*, 2007, **6**, 379-384.
5. S. Ji, H. Wang, T. Wang and D. Yan, *Adv. Mater.*, 2013, **25**, 1755-1760.
6. Y. Zang, F. Zhang, D. Huang, C.-a. Di, Q. Meng, X. Gao and D. Zhu, *Adv. Mater.*, 2014, **26**, 2862-2867.
7. A. P. F. Turner and N. Magan, *Nat. Rev. Microbiol.*, 2004, **2**, 161-166.
8. D.-J. Yang, I. Kamienchick, D. Y. Youn, A. Rothschild and I.-D. Kim, *Adv. Funct. Mater.*, 2010, **20**, 4258-4264.
9. A.-M. Andringa, J. R. Meijboom, E. C. P. Smits, S. G. J. Mathijssen, P. W. M. Blom and D. M. de Leeuw, *Adv. Funct. Mater.*, 2011, **21**, 100-107.
10. F. Schedin, A. K. Geim, S. V. Morozov, E. W. Hill, P. Blake, M. I. Katsnelson and K. S. Novoselov, *Nat. Mater.*, 2007, **6**, 652-655.
11. A.-M. Andringa, C. Piliego, I. Katsouras, P. W. M. Blom and D. M. de Leeuw, *Chem. Mater.*, 2014, **26**, 773-785.
12. S.-I. Ohira, P. K. Dasgupta and K. A. Schug, *Anal. Chem.*, 2009, **81**, 4183-4191.
13. S. Bai, C. Sun, T. Guo, R. Luo, Y. Lin, A. Chen, L. Sun and J. Zhang, *Electrochim. Acta*, 2013, **90**, 530-534.
14. J. S. Lee, O. S. Kwon, D. H. Shin and J. Jang, *J. Mater. Chem. A*, 2013, **1**, 9099-9106.
15. N. Pinna, G. Neri, M. Antonietti and M. Niederberger, *Angew. Chem. Int. Ed.*, 2004, **43**, 4345-4349.
16. M. E. Franke, T. J. Koplin and U. Simon, *Small*, 2006, **2**, 36-50.
17. L. C. Jia and W. P. Cai, *Adv. Funct. Mater.*, 2010, **20**, 3765-3773.
18. Y. Yang, C. Tian, J. Wang, L. Sun, K. Shi, W. Zhou and H. Fu, *Nanoscale*, 2014, **6**, 7369-7378.
19. M. R. Alenezi, S. J. Henley, N. G. Emerson and S. R. P. Silva, *Nanoscale*, 2014, **6**, 235-247.
20. S. Bai, T. Guo, Y. Zhao, R. Luo, D. Li, A. Chen and C. C. Liu, *J. Mater. Chem. A*, 2013, **1**, 11335-11342.
21. P. Sun, X. Zhou, C. Wang, K. Shimanoe, G. Lu and N. Yamazoe, *J. Mater. Chem. A*, 2014, **2**, 1302-1308.
22. H.-S. Woo, C.-H. Kwak, I.-D. Kim and J.-H. Lee, *J. Mater. Chem. A*, 2014, **2**, 6412-6418.
23. A. Tricoli and S. E. Pratsinis, *Nat. Nanotechnol.*, 2010, **5**, 54-60.

24. S. Deng, V. Tjoa, H. M. Fan, H. R. Tan, D. C. Sayle, M. Olivo, S. Mhaisalkar, J. Wei and C. H. Sow, *J. Am. Chem. Soc.*, 2012, **134**, 4905-4917.
25. S.-J. Choi, B.-H. Jang, S.-J. Lee, B. K. Min, A. Rothschild and I.-D. Kim, *ACS Appl. Mater. Interfaces*, 2014, **6**, 2587-2596.
26. F. Hernandez-Ramirez, J. Daniel Prades, A. Hackner, T. Fischer, G. Mueller, S. Mathur and J. Ramon Morante, *Nanoscale*, 2011, **3**, 630-634.
27. Z. Dai, Y. Li, G. Duan, L. Jia and W. Cai, *ACS Nano*, 2012, **6**, 6706-6716.
28. Z. Dai, L. Xu, G. Duan, T. Li, H. Zhang, Y. Li, Y. Wang, Y. Wang and W. Cai, *Sci. Rep.*, 2013, **3**, 1669.
29. Z. Dai, C.-S. Lee, B.-Y. Kim, C.-H. Kwak, J.-W. Yoon, H.-M. Jeong and J.-H. Lee, *ACS Appl. Mater. Interfaces*, 2014, **6**, 16217-16226.
30. K. J. Choi and H. W. Jang, *Sensors-Basel*, 2010, **10**, 4083-4099.
31. R. Lü, W. Zhou, K. Shi, Y. Yang, L. Wang, K. Pan, C. Tian, Z. Ren and H. Fu, *Nanoscale*, 2013, **5**, 8569-8576..
32. H. R. Kim, A. Haensch, I. D. Kim, N. Barsan, U. Weimar and J. H. Lee, *Adv. Funct. Mater.*, 2011, **21**, 4456-4463.
33. N. Wang, C. G. Hu, C. H. Xia, B. Feng, Z. W. Zhang, Y. Xi and Y. F. Xiong, *Appl. Phys. Lett.*, 2007, **90**, 163111.
34. L. A. Patil, A. R. Bari, M. D. Shinde, V. Deo and M. P. Kaushik, *Sens. Actuators, B*, 2012, **161**, 372-380.
35. M. B. Mitchell, V. N. Sheinker, W. W. Cox and K. Hardcastle, *J. Phys. Chem. C*, 2011, **115**, 11514-11524.
36. J. Shin, S.-J. Choi, I. Lee, D.-Y. Youn, C. O. Park, J.-H. Lee, H. L. Tuller and I.-D. Kim, *Adv. Funct. Mater.*, 2013, **23**, 2357-2367.
37. X. J. Huang, Y. F. Sun, L. C. Wang, F. L. Meng and J. H. Liu, *Nanotechnology*, 2004, **15**, 1284-1288.
38. Y. C. Lee, Y. L. Chueh, C. H. Hsieh, M. T. Chang, L. J. Chou, Z. L. Wang, Y. W. Lan, C. D. Chen, H. Kurata and S. Isoda, *Small*, 2007, **3**, 1356-1361.
39. H. Huang, H. Gong, C. L. Chow, J. Guo, T. J. White, M. S. Tse and O. K. Tan, *Adv. Funct. Mater.*, 2011, **21**, 2680-2686.
40. P. T. Moseley, *Meas. Sci. Technol.*, 1997, **8**, 223-237.
41. A. Gurlo, M. Sahm, A. Oprea, N. Barsan and U. Weimar, *Sens. Actuators, B*, 2004, **102**, 291-298.
42. A. Gurlo, N. Barsan, A. Oprea, M. Sahm, T. Sahm and U. Weimar, *Appl. Phys. Lett.*, 2004, **85**, 2280-2282.
43. J. X. Wang, X. W. Sun, Y. Yang and C. M. L. Wu, *Nanotechnology*, 2009, **20**, 465501.
44. F. Q. Sun, W. P. Cai, Y. Li, L. C. Jia and F. Lu, *Adv. Mater.*, 2005, **17**, 2872-2877.
45. Z. Dai, L. Jia, G. Duan, Y. Li, H. Zhang, J. Wang, J. Hu and W. Cai, *Chem.-Eur. J.*, 2013, **19**, 13387-13395.
46. S. Thirumalairajan, K. Girija, N. Y. Hebalkar, D. Mangalaraj, C. Viswanathan and N. Ponpandian, *RSC Adv.*, 2013, **3**, 7549-7561.
47. X. Hu, J. C. Yu, J. Gong, Q. Li and G. Li, *Adv. Mater.*, 2007, **19**, 2324-2329.
48. W. Robert and S. MingáYang, *Chem, Commun.*, 2003, **6**, 688-689..
49. I. Giebelhaus, E. Varechkina, T. Fischer, M. Rumyantseva, V. Ivanov, A. Gaskov, J. R. Morante, J. Arbiol, W. Tyrra and S. Mathur, *J. Mater. Chem. A*, 2013, **1**, 11261-11268..
50. I.-D. Kim, A. Rothschild, B. H. Lee, D. Y. Kim, S. M. Jo and H. L. Tuller, *Nano Lett.*, 2006, **6**, 2009-2013.
51. D. H. Zhang, Z. Q. Liu, C. Li, T. Tang, X. L. Liu, S. Han, B. Lei and C. W. Zhou, *Nano Lett.*, 2004, **4**, 1919-1924.
52. J. X. Yi, S. J. Feng, Y. B. Zuo, W. Liu and C. S. Chen, *Chem. Mater.*, 2005, **17**, 5856-5861.
53. Y. Asano and K. Fuchizaki, *J. Chem. Phys.*, 2012, **137**, 174502.
54. H. Wang, K. Dou, W. Y. Teoh, Y. Zhan, T. F. Hung, F. Zhang, J. Xu, R. Zhang and A. L. Rogach, *Adv. Funct. Mater.*, 2013, **23**, 4847-4853.
55. P. Rai, Y.-S. Kim, H.-M. Song, M.-K. Song and Y.-T. Yu, *Sens. Actuators, B*, 2012, **165**, 133-142.
56. M. Iwamoto, Y. Yoda, N. Yamazoe and T. Seiyama, *J. Phys. Chem.*, 1978, **82**, 2564-2570.
57. H.-J. Kim and J.-H. Lee, *Sens. Actuators, B*, 2014, **192**, 607-627.

Graphical Table of Contents

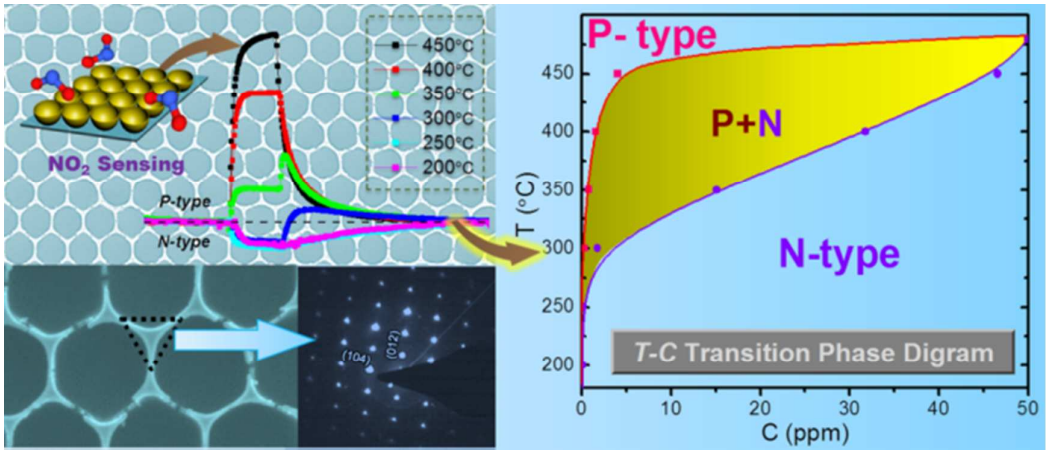

Monolayer α-Fe_2O_3 inverse opal with single-crystalline rotocenters shows the reversible NO_2 p-n sensing switches tuned by a *T-C* transition diagram.